3D RoboMET™ Characterization

Jonathan D. Madison [1851], Donald Susan [1831], Alice Kilgo [1819]
Sandia National Laboratories
Albuquerque, NM 87185

Abstract

The goal of this project is to generate 3D microstructural data by destructive and non-destructive means and provide accompanying characterization and quantitative analysis of such data. This work is a continuing part of a larger effort to relate material performance variability to microstructural variability. That larger effort is called "Predicting Performance Margins" or PPM. In conjunction with that overarching initiative, the RoboMET.3D™ is a specific asset of Center 1800 and is an automated serial-sectioning system for destructive analysis of microstructure, which is called upon to provide direct customer support to 1800 and non-1800 customers. To that end, data collection, 3d reconstruction and analysis of typical and atypical microstructures have been pursued for the purposes of qualitative and quantitative characterization with a goal toward linking microstructural defects and/or microstructural features with mechanical response. Material systems examined in FY15 include precipitation hardened 17-4 steel, laser-welds of 304L stainless steel, thermal spray coatings of 304L and geological samples of sandstone.

Introduction

Description of microstructure in three-dimensions is an emerging and rapidly developing area of study within the field of materials science & engineering. There currently exist a broad array of experimental tools geared toward interrogating microstructure in three-dimensions, with some methods being destructive [1-5] and others non-destructive[6-9]. In this project, two methods: one destructive and one non-destructive, are utilized to obtain details of microstructural arrangements under varied processing conditions and to investigate microstructural defects in these material systems. The methods employed in this project are micro-computed tomography and automated serial-sectioning.

Approach

Using micro-computed tomography capabilities from staff in 1522 and automated serial-sectioning with the RoboMET.3D™ system, a variety of investigations were performed to relate mechanical performance with observable microstructural changes. Resolution limits for micro-computed tomography are typically on the order of 10 – 20 μm per voxel edge while automated serial-sectioning with the RoboMET.3D™ system has demonstrated resolutions as low as 1-2 um per slice. This fiscal year, features observed with computed tomography have focused on casting and processing porosity in laser welds whereas RoboMET.3D™ investigations have been largely focused on multi-phase assemblies of metals or geological formations.

Results and Impacts

1. Casting Porosity in 17-4 PH Stainless Steel

1.1. Specific Method

Investment cast tensile bars were investigated in this work having square cross-sections (0.1 x 0.2 x 1.0 in) or round cross-sections (0.25 in dia x 1.0 in). Heat treatments were then imposed on the rectangular bars at either an H925 or H1025 condition. The round bars were heat treated to H925, H1025, or an H1100 temper. Mechanical tensile testing was pursued at strain rates and temperatures corresponding to conditions where brittle failure has been observed in cast components utilizing this alloy or a compositionally similar derivative. During mechanical testing, intentional, intermittent interruptions were introduced to allow micro-computed tomography to identify general locations of pore content and the extent of internal porosity growth over increasing plastic strains. See Figure 1 for a set of representative interrupted tensile test curves for samples at the H1100 and H925 heat treatments. During this period, rectangular tensile bars displayed porosity both in the interior of the gage section as well as along specimen edges, whereas the cast round bars generally contained porosity only along the centerline of the sample, which primarily increased in size within locations of pronounced necking. For an example of void growth in one round tensile bar during deformation, see Figure 2.

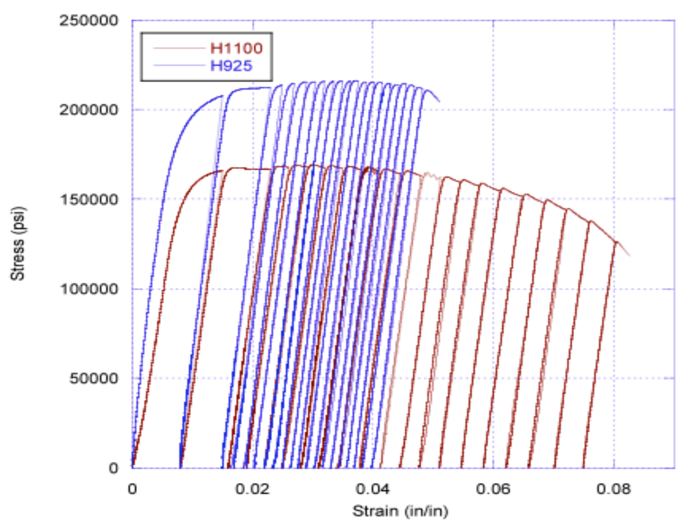

Figure 1 - Representative stress vs. strain curves for interrupted tensile tests for a sample heat treated at H1100 and H925 conditions

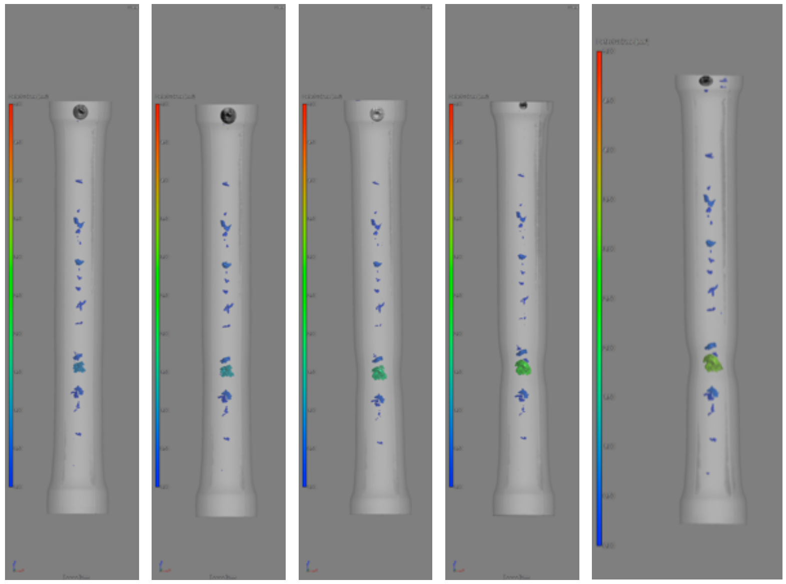

Figure 2 - micro-CT results of a round cast tensile throughout an interrupted tensile test

1.2. Results

Using micro-computed tomography results, traditional metallography were pursued in the regions of high pore content, which most often coincided with the regions of greatest deformation with fractography also being pursed at failure sites. Among both location types, porosity content was measured by quantitative image analysis (QIA) on polished cross-sections using the Clemex PE image analysis system and characterized via fracture surfaces of broken tensile bars using scanning electron microscopy (SEM) in a Zeiss Supra 55VP SEM. Figure 3 shows representative examples of casting voids and interconnected fracture surfaces in one of the round tensile specimens. Lastly, it is important to specify that all porosity measures derived from all fracture surfaces are the apparent or projected area percentages, not a surface area, as surface roughness was not taken into account in this analysis.

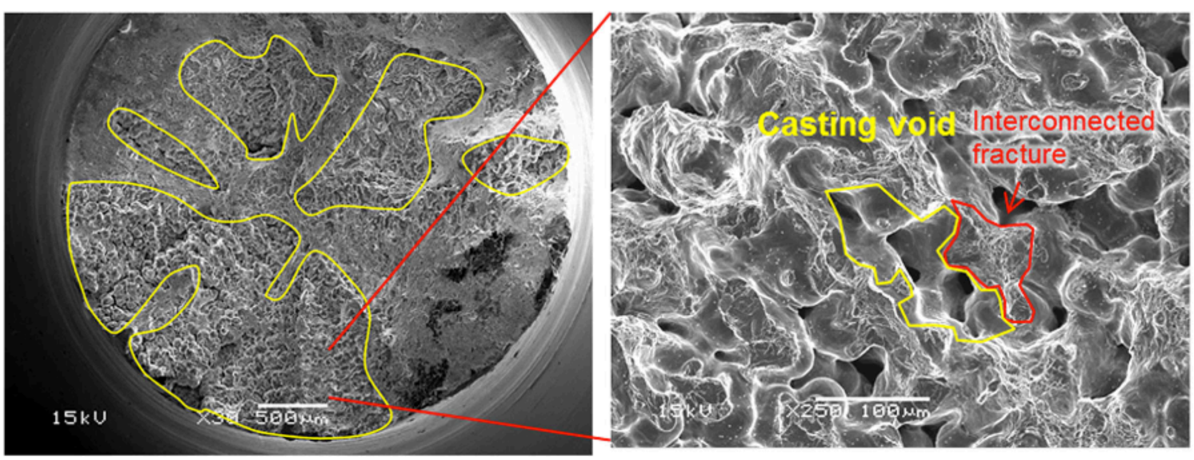

(a) (b)

Figure 3 - Representative fracture surfaces from a round cast tensile bar

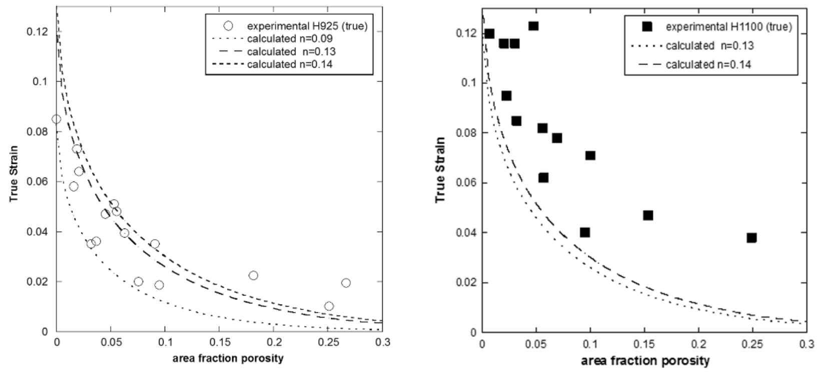

(a) (b)

Figure 4 - True Strain vs. Area Fraction Porosity for both experiment and the Cáceres Model for cast PH 17-4 under heat-treatments of (a) H925 and (b) H1100

1.3. Impact/Significance

After consideration of a large number of tested cast tensile bars and extensive metallography, it was found that the tensile behavior of cast PH 17-4 correlates to the local porosity, measured on fracture surfaces, but does not relate well to the overall (bulk) porosity in the material. The yield strength and ultimate tensile strength decrease moderately due to the presence of voids, roughly in proportion to the reduction in load bearing cross-sectional area. In contrast, the effect of porosity on ductility is more severe, with approximately an 80% decrease in failure strain for 10% porosity located at the failure surface. Additionally, tensile testing at decreased temperatures tends to exacerbate reductions on ductility

Quantitative analyses of the true failure strain versus area fraction porosity were obtained with a critical local strain model, developed by Cáceres et al[10,11], which showed reasonable agreement between calculated and experimental failure strains for castings in the H925 condition. The H1100 material displays more necking, with non-uniform strain contributing more to the overall failure strain thereby indicating a greater than predicted impact of local porosity. Because of this, the critical strain model did not correlate well with the experimental results for the H1100 condition. See Figure 4.

This work and all its relevant details are captured in the following publication:

- D.F. Susan, T.B. Crenshaw, J.S. Gearhart, "The effects of casting porosity on the tensile behavior of investment cast 17-4PH stainless steel", **J. Mater. Engr. & Perf.,** 24, 2917-2923, 2015.[12]

2. Laser Weld Porosity in Vacuum Arc Remelted 304L Stainless Steel

2.1. Specific Method

Autogeneous laser butt welds of vacuum arc remelted 304L plates were performed for a variety of partial penetrations using two companion weld schedules (α and β) which produce welds with an equivalent volumetric footprint at each penetration depth. In an effort to couple the impact of process-induced porosity content on mechanical performance, micro-computed tomography on tensile samples machined from these plates were pursued for welds having penetration depths of 0.03 in. (0.762 mm), 0.04 in. (1.016 mm), 0.05 in. (1.27 mm) and 0.06 in. (1.524 mm) under weld schedule α and β.

Additionally, in order to begin to treat the influence of geometric variation on weld performance in a controlled and methodical manner, welds having a gap width of 0.0 in. (0.0 mm), 0.004 in. (0.1016 mm), and 0.010 in. (0.254 mm) and a uniform penetration depth of 0.05 in. (1.27 mm) were also examined. As a material system of interest for welds and weld re-designs in the B61 and W88, the interplay between geometric tolerances, porosity and weld schedule are of prime importance particularly when examined in conjunction with their effect on mechanical performance and resilience.

2.2. Results

Population metrics as determined by three-dimensional reconstruction for porosity content in each weld are reported below and are presented as equivalent spherical diameter pore histograms for a given weld schedule depth (Fig. 5) and gap size (Fig. 6). The legend and color series indicate which population distribution was produced under weld α or β. As can be observed from Figures 5, at each penetration depth, while mean void size and void size distribution between both weld schedules are quite similar across all cases, weld schedule α consistently produced greater amounts of porosity than schedule β by approximately a factor of 2. It should also be noted, as penetration depths increase, total void count, void frequency and void volume fraction also increased for both weld schedules. With regards to gapped welds, the same trend of having approximately twice the porosity content in α welds compared to β welds held true for all investigated gapped widths as well.

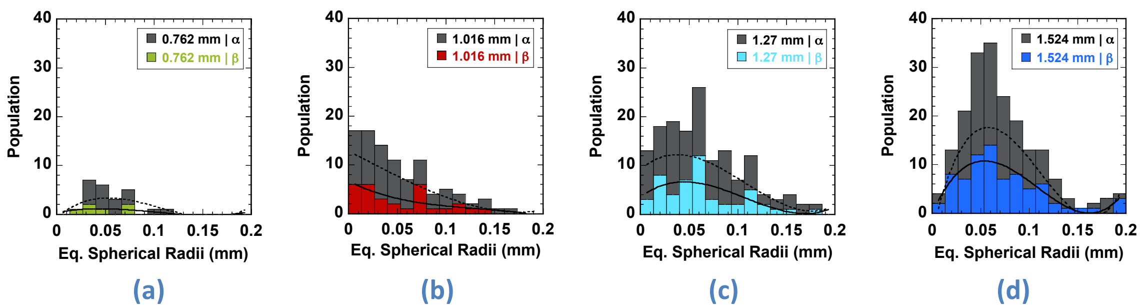

Figure 5 – Equivalent spherical radii distributions for non-gapped welds under weld schedule α and β for penetration depths of (a) 0.762 mm, (b) 1.016 mm, (c) 1.27 mm and (d) 1.524 mm

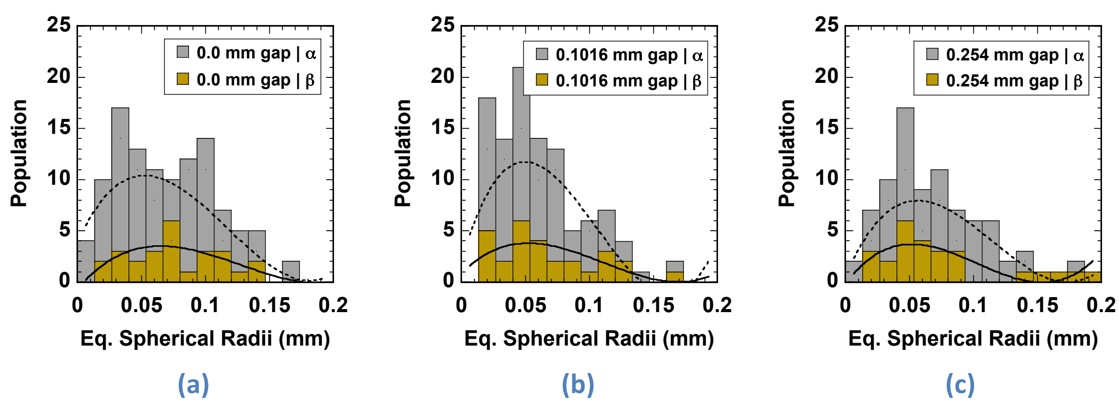

Figure 6 - Equivalent Spherical Radii distributions for gapped weld cases under weld schedule α and β having a uniform penetration depth of 1.27 mm with initial weld gap of (a) 0.0 mm (b) 0.1016 mm and (c) 0.254 mm

This explicit porosity characterization was then coupled with tensile mechanical testing of the specific samples from which the pore structure was examined. Samples were tested to failure with high resolution multi-camera observation for digital image correlation of local and global displacement and strain. Results of mechanical testing on the porosity containing non-gapped and gapped welds described in Figures 5 and 6 can be found in Figures 7 and 8.

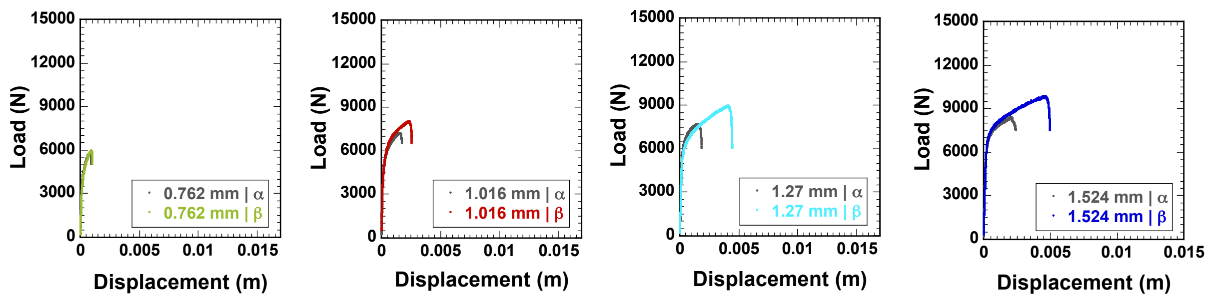

(a) (b) (c) (d)

Figure 7 - Load Displacement Curves for α and β weld schedules at weld penetration depths of (a) 0.762 mm, (b) 1.016 mm, (c) 1.27 mm and (d) 1.524 mm with no gap.

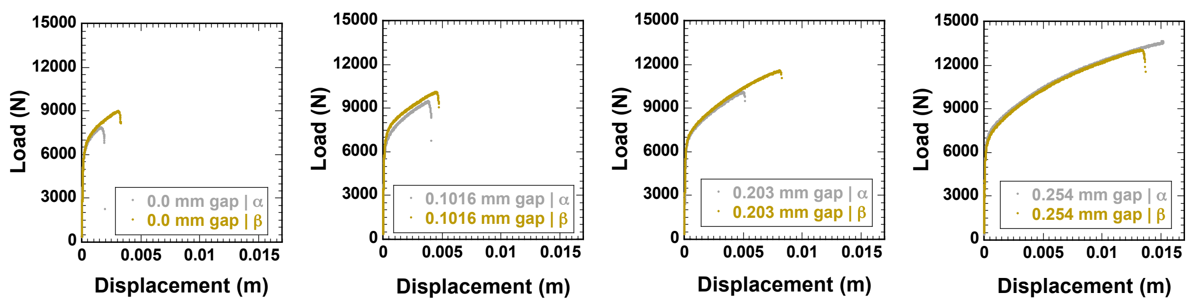

(a) (b) (c) (d)

Figure 8 - Load Displacement Curves for α and β weld schedules at a fixed penetration depth of 1.27 mm and initial gap size of (a) 0.0 mm, (b) 0.1016 mm, (c) 0.2032mm and (d) 0.254 mm

2.3. Impact/Significance

When considered separately, both gapped and non-gapped autogeneous laser-welds of 304L VAR reveal changes in porosity presence can be correlated to sizeable changes in mechanical response. However, when the behaviors of gapped and non-gapped autogeneous laser welds are considered together, the scalability of mechanical response appears to lie within two regimes. This is illustrated in Figures 9 and 10. In an effort to incorporate multiple measures into a single metric, one may be encouraged to scale the average void volume by the void frequency. This will produce a measure in units of length^2 and provide an estimate of the cross-sectional area occupied by voided regions throughout the length of the linear autogenous weld. Here we will denote this measure as “nominal average area through volume” or “NAATV”. As shown in Figure 9, NAATV is plotted against total displacement to failure for all welds investigated. This measure shows a relatively clear demarcation between gapped and non-gapped welds with non-gapped welds demonstrating lower displacements to failure across all calculations of NAATV save one case, which possesses an "NAATV" of 0.0138 and a displacement to failure of 3.86 mm. While this measure provides clear separation between most gapped and non-gapped samples, there is little readily apparent to justify the outlier. However, by taking the average of the raw three-dimensional measures of pore volume directly from the 3d reconstructions, a clearer delineation between gapped and non-gaped welds, free of outliers, is seen when plotted against peak load at failure.

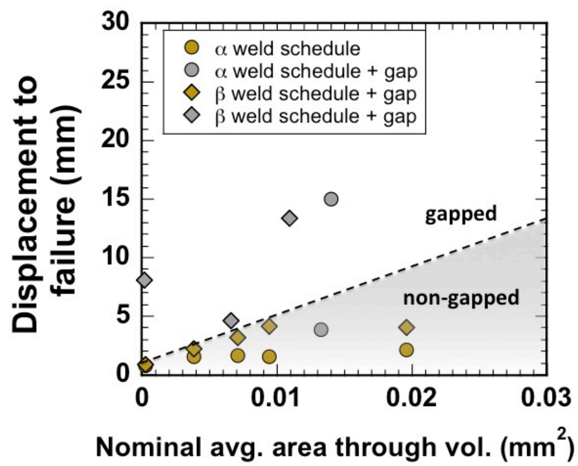

Figure 9 - Displacement to failure as a function of nominal average area through the volume, again showing extreme tendency for gapped welds to sustain greater far-field displacements to failure irrespective of their relative voided space within the weld

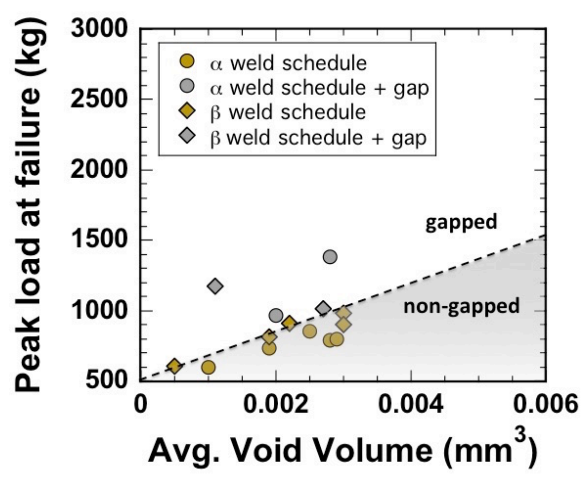

Figure 10 - Peak Load at failure as a function of average void volume per weld. Across all weld cases, gapped welds sustained higher peak loads regardless of the average void size present.

This work and all its relevant details are captured in a manuscript in draft for Met Trans A:

- J. Madison, H. Jin, J. Foulk, S. Murawski, C. Robino, "New Microstructural Insights to the Constitutive Behavior of Laser Welds in 304L Stainless Steel – I" *in preparation*

3. Volumetric Deformation in Thermal Spray Coatings of 304 Stainless Steel

3.1. Specific Method

Thermal spray technology is a long-standing coating technique with a variety of specific, high value applications. Researchers in Organizations 1526 and 1832 have been exploring approaches to augment the dissipative properties of surfaces by altering the contact interface. Specifically much work has been done to more clearly understand the plastic and viscous response of a thermal spray coating under carefully controlled impact events[13-16]. To assist in this endeavor, the RoboMET.3D™ was employed to collect multiple serial-sectioning experiments on impact tested thermal spray coatings from which changes in the coefficient of restitution was measured as a function of impact velocity and impact quantity. See Figure 11 for experimental impact setup and coefficient of restitution measurements. Serial-sectioning experiments were undertaken for three consistencies of thermal sprayed 304 stainless steel atop a substrate of 304. For the purposes of this report, the three grades shall be denoted as "dense", "average" and "porous". Each serial-sectioning experiment consisted of no less than 400+ slices per sample with the three primary experiments being performed on thermal spray cross-sections having nominal cross-sections in the range of 10 – 20 mm in length and 1 mm in width.

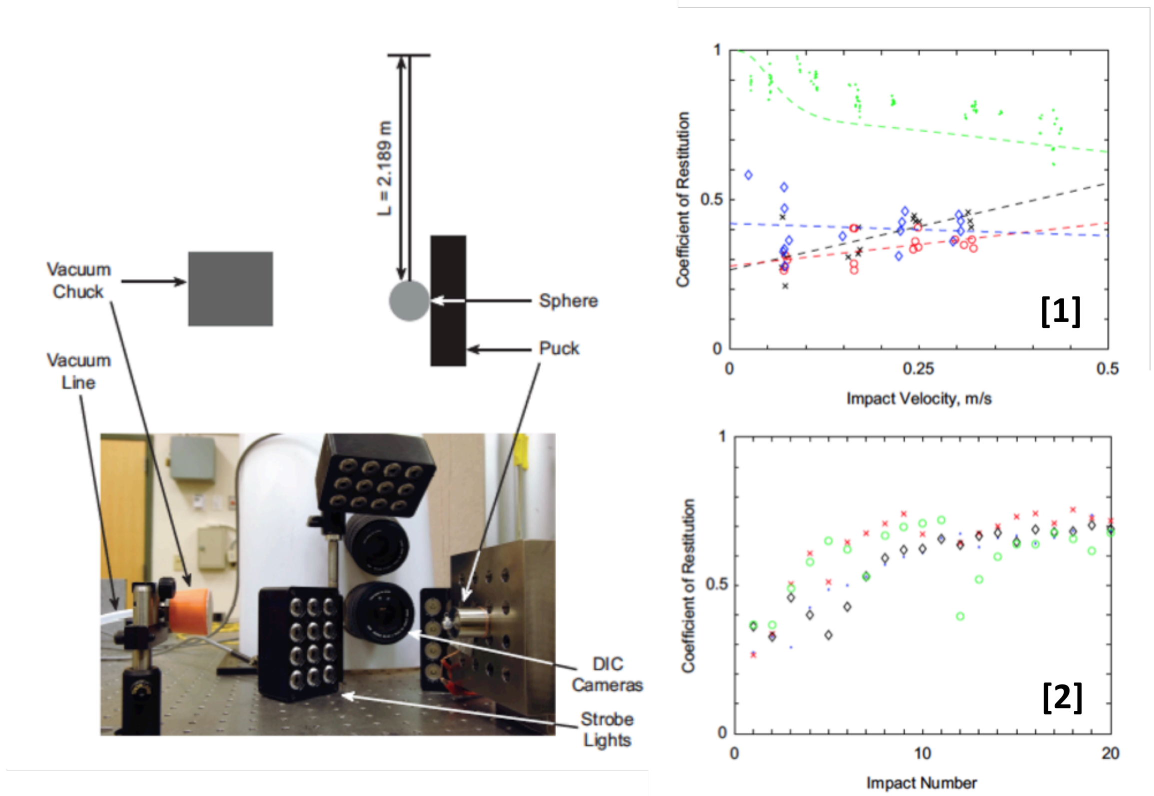

(a) (b)

Figure 11 - (a) Schematic and photo of impact testing experiment and (b) coefficient of restitution measurements as functions of [1] impact velocity and [2] impact number

3.2. Results

The removal rates for the three primary serial-sectioning experiments are shown below. See Figure 12. Below. For each experiment the removal rate was determined by two independent measures. The first measure is calculated by the average focus height across all tiles of the montage for each slice. The second measure is acquired by laser interferometer at discrete intervals throughout the serial-sectioning experiment. For details of the serial-sectioning experiments including montage tile count, total number of sections and total reconstructed volume, see Table 1.

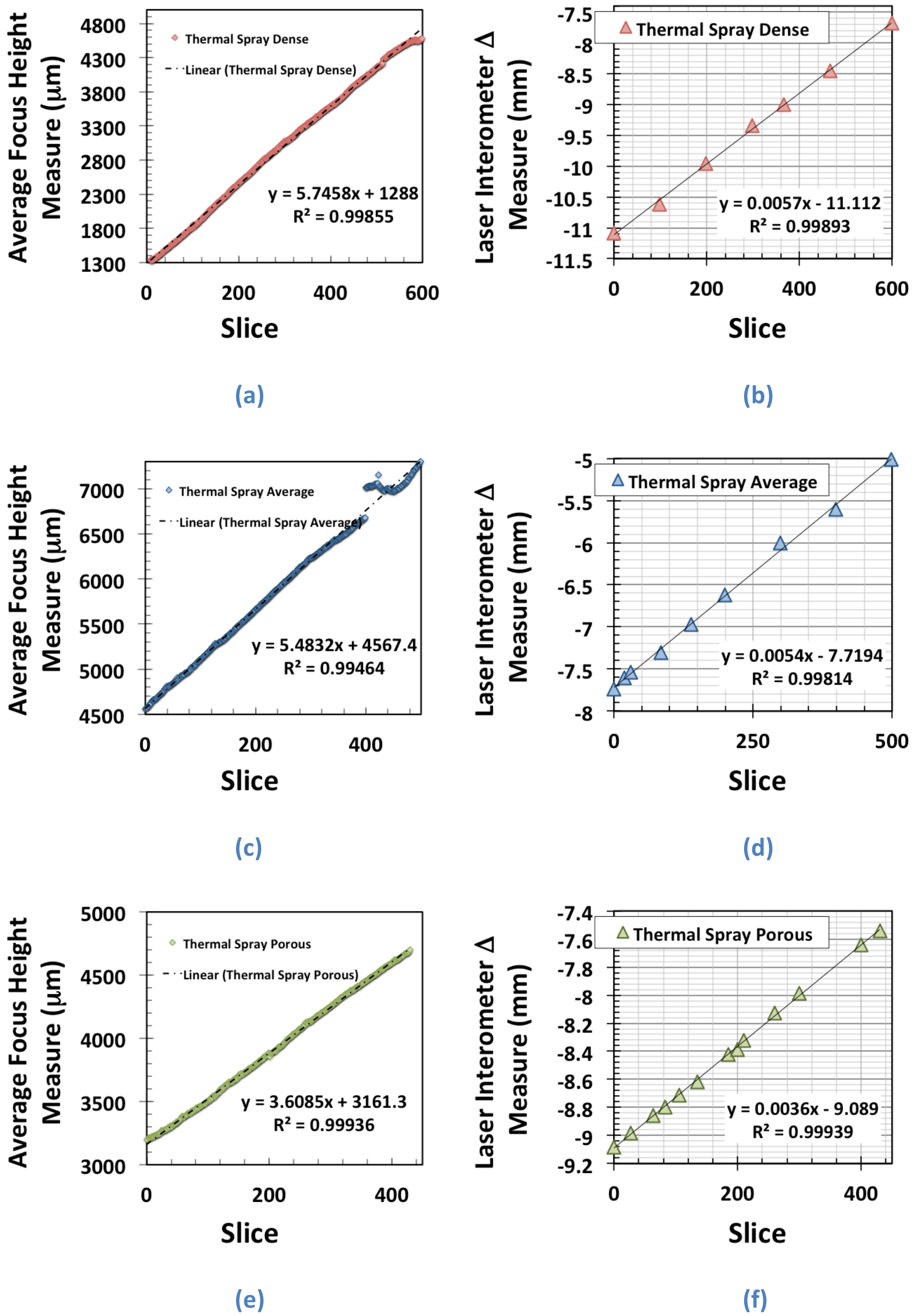

Figure 12 - Dual Method Material Removal Measures by Montage Focus Height (a, c, & d) and Laser Interferometer (b, d & e) for "dense", "average", and "porous" thermal spray samples.

Table 1 - Details of Thermal Spray Serial-Sectional Experiments and Reconstructions

Thermal Spray Consistency	Image Magnification	Montage Dimensions (Total Tile Count)	Total # of Serial-Sections Acquired	Total Volume Reconstructed (mm x mm x mm)
“Dense”	20X	20 x 2 (40)	515	14.2 x 1.1 x 2.9
“Average”	20X	32 x 2 (64)	500	21.6 x 1.1 x 2.8
“Porous”	20X	18 x 3 (54)	430	10.0 x 1.2 x 1.5

3.3. Impact/Significance

It was determined, regardless of the observed changes in coefficient of restitution, damage regions of thermal spray coatings were limited to the outer portion of the coating’s surface. Multiple views of a 3d reconstruction from a “porous” sample are shown below in Figure 13. Figure 13(b) illustrates one such damage region where disturbance to the microstructure is limited to the surface of the coating. These observations were confirmed by interrogating hundreds of 2d cross-sections along the height (*y*-axis in Figure 13) of the thermal spray coatings. See Figure 14. These micrographs reveal the morphology of the spray coating at a series of heights with each image separated by approximately 30 microns. Images depicted are of the xz plane proceeding in the -y direction beginning above the thermal spray coating and continues into the coating’s interior. As illustrated by arrows, surface depressions present at locations of near uniformity in the remainder of the coating dissipate after 30 – 60 microns. This behavior was observed throughout and across all 3d reconstructions. These cross-sections show negligible disturbance to thermal spray microstructures, in terms of local depressions beyond what is expected from the typical coating roughness.

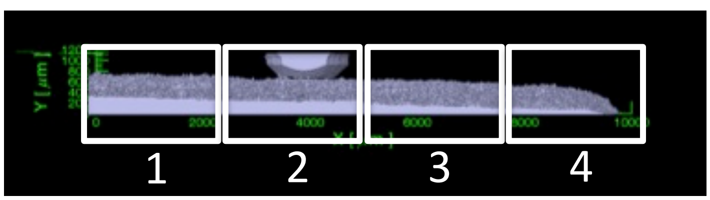

(a)

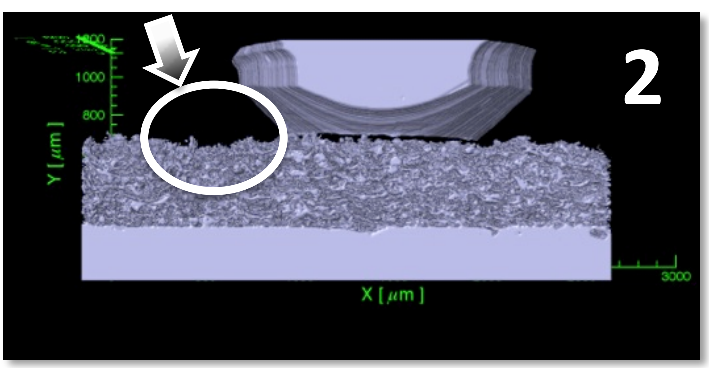

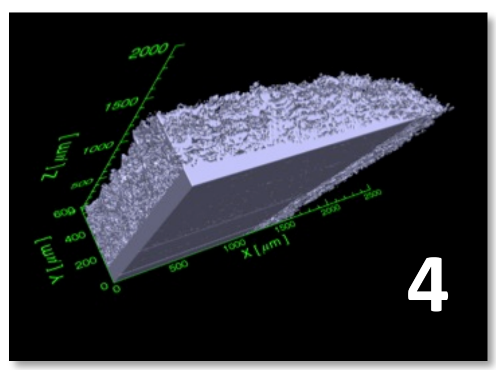

(b) (c)

Figure 13 - 3d Reconstruction of "porous" thermal spray sample. (a) entire reconstruction (b) cropped volume from entire reconstruction showing a damage region resulting from impact testing and (c) a cropped volume from the entire reconstruction demonstrating the sloped nature of the thermal spray samples at their trailing edge.

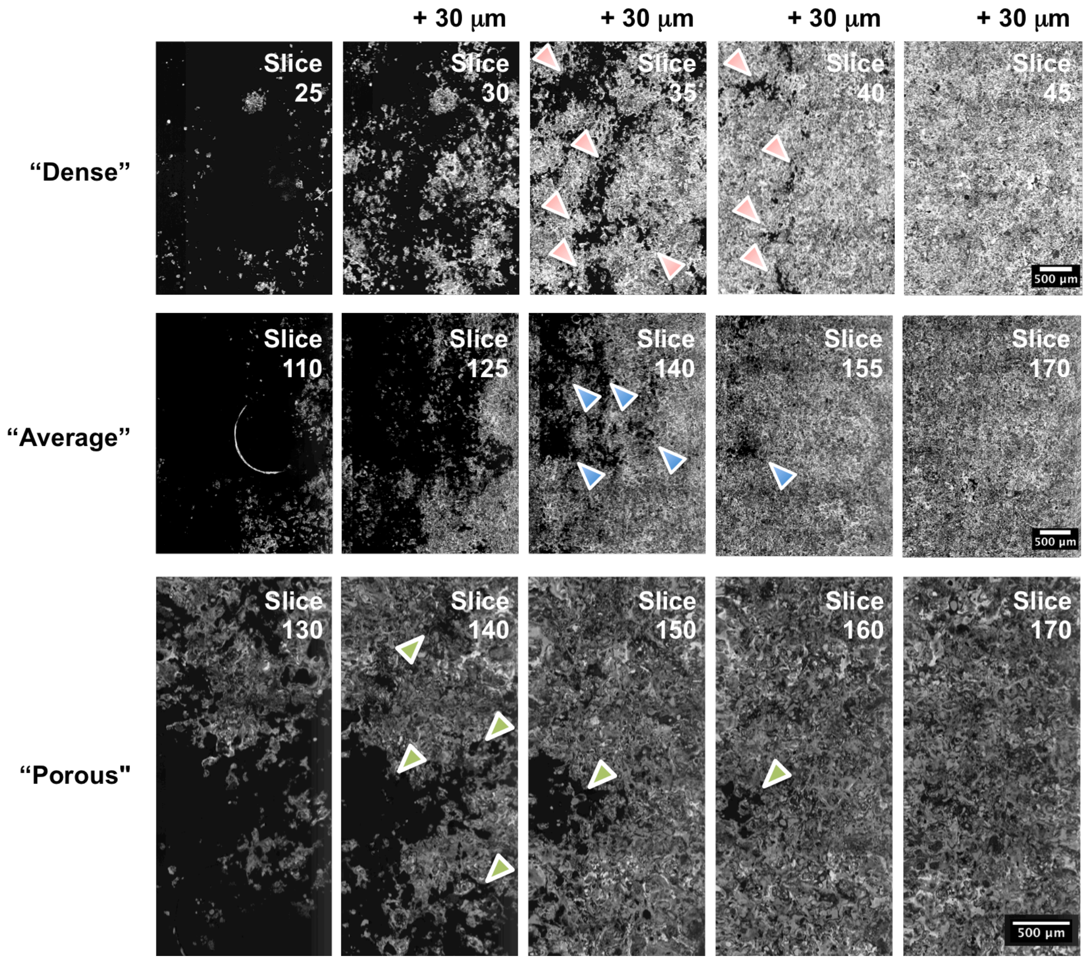

Figure 14 - Series of 2D micrographs in 30 μm intervals along the height (*y*-axis) of each thermal spray sample type revealing localized surface depressions and their nominal depths. Large depressions observed beyond the typical roughness of the thermal spray coating subside after one to two intervals of 30 μm.

These findings suggest impact damage to the thermal sprays are negligible when considered in the scope of spray thicknesses on the order of 0.5 mm or greater, for the impact regimes investigated. This in turn supports the hypothesis that consistency in properties and performance following repeated impacts at the scale and quantity of the impact testing scenarios are a reasonable expectation.

4. Spatial Distribution of Quartz Crystals in Geological Formations

4.1. Specific Method

Naturally occurring formations of rock, clay, sand and other minerals are an integral factor in the extraction of gas and oil from shale. Recent work in the geological community has focused heavily on three-dimensional characterization and analysis of pores, pore networks and flow behavior in these formations. Many of these efforts have utilized dual-beam focused ion beam or diffraction methods to interrogate and obtain three-dimensional structures for analysis [17-19]. While effective in certain cases, the length-scales of such methods are either primarily amenable to very small volumes (e.g. FIB) or largely dependent on local contrasts in density for identification of features (e.g. diffraction techniques).

To acquire more appreciable volumes in larger scale systems the RoboMET.3D™ was employed. A circular-plate sample of quartz crystals infiltrated with clay and voids, embedded in a rhodamine epoxy having a radial diameter of 2.5 cm and a thickness of 0.5 cm was serial-sectioned in two experiments. One experiment took the entire sample cross-section as the region of interest. The second experiment took one quarter of the sample as the region of interest affording the opportunity to image the sample at a higher resolution and effectively serial-section through a greater thickness given the same time investment. Metallographic preparation for both samples was nearly equivalent with minor changes made only to account for the smaller cross-sectional area of the secondary sample. This resulted in rather uniform material removal rates between both samples.

4.2. Results

To differentiate the samples, we will denote the initial experiment as "Quartz Whole" and the second experiment as "Quartz Quarter". Total through-thickness sectioning depth for the "whole" sample was approximately 1.5 mm while the through-thickness for the "quarter" sample was just over 2.5 mm. The experimental removal rates per slice are shown in Figures 15. Optical images of a single serial-section from each experiment are shown in Figure 16.

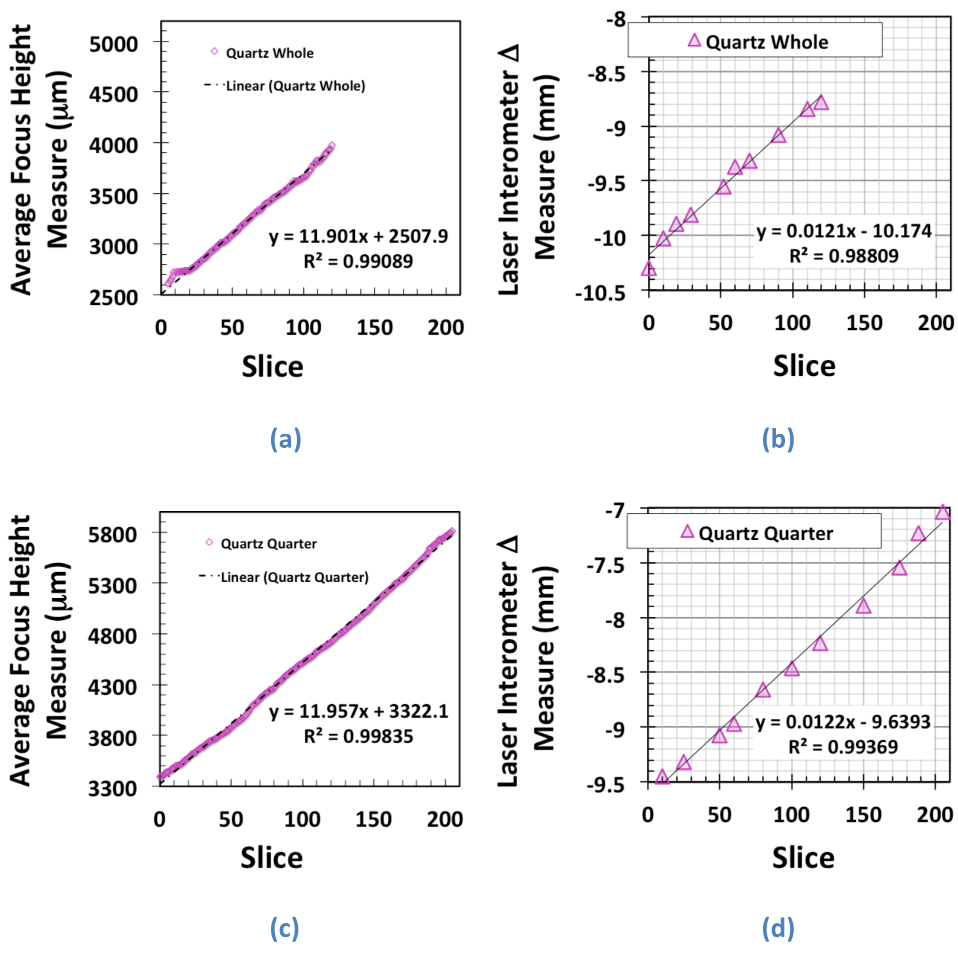

Figure 15 - Dual Method Material Removal Measures by Montage Focus Height (a & c) and Laser Interferometer (b & d) for both Quartz serial-section experiments.

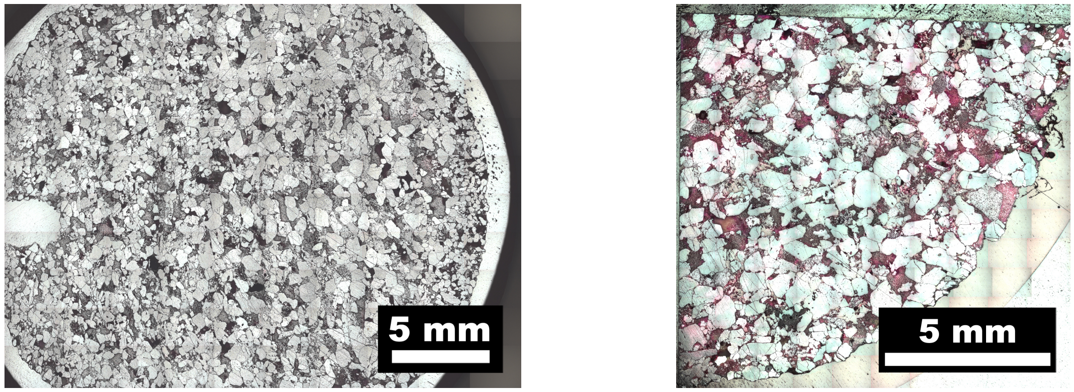

(a) (b)

Figure 16 - Single Slice Optical Micrograph Raw Data for (a) "whole" and (b) "quarter" Quartz serial sectioning experiments

Using image processing to remove imaging artifacts and isolate the surrounding clay and epoxy, the quartz was segmented as a singular phase. This allowed for initial 3d visualization for quartz with all other features removed from view. See Figure 17. Planar area fraction measures from one quarter of the sample were then pursued to quantify the local variation in quartz presence throughout the reconstructed volume. See Figure 18. The global decrease in the measure is indicative of the curved edges of the sample giving way to decreasing cross-sectional areas as you traverse increasing lengths on the x and y axes. The local variation however show fluctuations in area fraction over very small distances (< 1 mm) in the range of ± 10-20%.

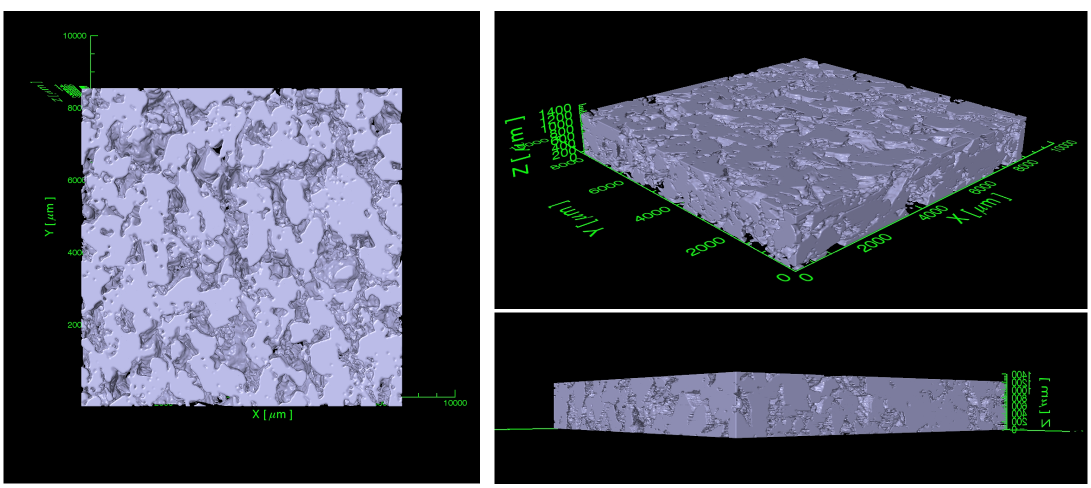

Figure 17 - 3D reconstruction of Quartz with epoxy and clay extracted from view

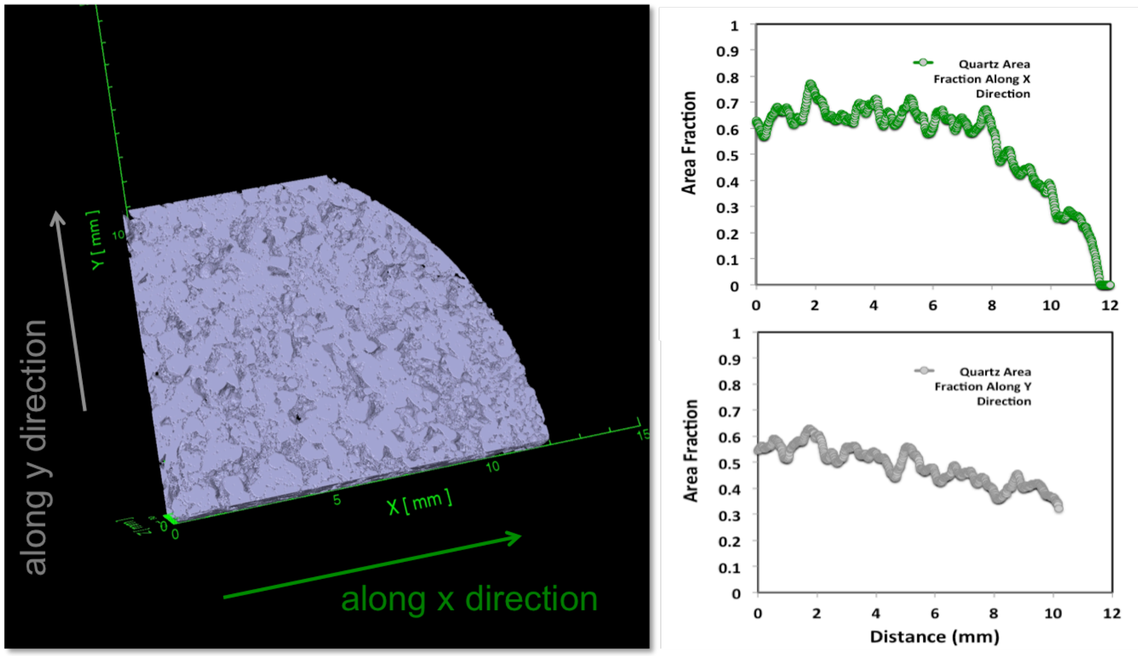

Figure 18 - 3D reconstruction from one quarter of "whole" sample with area fraction measures along the x direction and y direction illustrating local variation in quartz presence through volume

4.3. Impact/Significance

Using the RoboMET.3D™, much larger volumes of geological networks have been explored and reconstructed as compared to commonly employed techniques such as focused-ion beam or diffraction methods. Reconstructions show large fluctuations in area fraction over very small distances. Additionally, the second data set collected holds promise for the application of multi-threshold segmentations to identify quartz, clay, sand, epoxy and voids simultaneously. To that end, multi-phase 3dimensional identification will allow these reconstructions to be used to determine channel connectivity and will allow segmented reconstructions to be used as inputs for fluid flow models to determine flow permeability in this arrangement of sandstone.

Conclusions and Future Work

This fiscal year, destructive and non-destructive materials investigations were conducted in four primary areas. Non-destructive investigations utilized micro-computed tomography to identify; 1) void growth and coalescence in precipitation-hardened 17-4 cast steels, 2) porosity in laser-welds of 304L stainless steel while destructive investigation used mechanical serial-sectioning via the RoboMET.3D™ to interrogate; 3) spatial extents of damage in thermal spray coatings of 304L and 4) geological formations of sandstone containing large quantities of quartz and other packing materials.

Non-destructive investigations enabled direct linking of internal defect fields with mechanical response. In the case of PH 17-4, it was found that the effect of porosity on ductility can be rather severe, with approximately an 80% decrease in failure strain for 10% porosity content located at the failure surface. In the case of gapped and non-gapped laser welds of 304L stainless steel, pore content maintains an inverse relationship with displacement to failure and peak load to failure with gapped welds having notably better mechanical response when compared with non-gapped partial penetration laser welds having a near equivalent volumetric footprint across all pore content amounts.

Destructive investigations showed impact damage regions for investigation of the coefficient of restitution in thermal sprays were limited to less 0.1 mm of the thermal spray surface. Furthermore, geological formations of sandstone were revealed very large fluctuations, on the order of ± 10-20%, in local area fraction of quartz over distances of less than 1 mm.

Future work will focus on examining porosity in laser welds under multiple strain rates and temperatures, multi-phase thresholding of geological formations for input into fluid flow models, process-related defect fields in additive manufacturing, tension-induced voids in high purity bcc metals and cracks in glass to meal seals.

Summary of Findings and Capabilities Related to Aging

No findings relevant to specific component/material aging or capabilities were obtained this year.

References

[1] J. Spowart: *Scripta Mater.*, 2006, vol. 55 (1), pp. 5-10.
[2] D. Kammer and P. W. Voorhees: *MRS Bull.*, 2008, vol. 33 (6), pp. 603-09.
[3] G. Spanos, D. J. Rowenhorst, A. C. Lewis and A. B. Geltmacher: *MRS Bull.*, 2008, vol. 33 (6), pp. 597-602.
[4] A. Ullah, G. Liu, J. Luan, W. Li, M. Rahman and M. Ali: *Mater. Char.*, 2014, vol. 91 pp. 65-75.
[5] M. P. Echlin, A. Mottura, C. J. Torbet and T. M. Pollock: *Rev. Sci. Instr.*, 2012, vol. 83 pp. 023701-1 - 6.
[6] J.-Y. Buffiere, P. Cloetens, W. Ludwig, E. Maire and L. Salvo: *MRS. Bull.*, 2008, vol. 33 (6), pp. 611-19.
[7] D. Juul Jensen, S. E. Offerman and J. Sietsma: *MRS Bull.*, 2008, vol. 33 (6), pp. 621-29.
[8] M. Suery, S. Terzi, B. Mireux, L. Salvo, J. Adrien and E. Maire: *JOM*, 2012, vol. 64 (1), pp. 83-88.
[9] H. A. Bale, A. Haboub, A. A. MacDowell, J. R. Nasiatka, D. Y. Parkinson, B. N. Cox, D. B. Marshall and R. O. Ritchie: *Nat. Mater.*, 2012, vol. 12 pp. 40-46.
[10] C. H. Cáceres and B. I. Selling: *Scripta Met. Mater.*, 1995, vol. 32 (11), pp. 1851-56.
[11] C. H. Cáceres and B. I. Selling: 1996, vol. A220 (1-2), pp. 109-16.
[12] D. F. Susan, T. B. Crenshaw and J. S. Gearhart: *J. Mat. Engr. & Perf.*, 2015, vol. 24 (8), pp. 2917-24.
[13] M. R. Brake: *Nonlin. Dynam.*, 2014, vol. 77 pp. 899-922.
[14] M. R. Brake: *Int. J. Sol. & Struct.*, 2012, vol. 49 pp. 3129-41.
[15] A. C. Hall, D. J. Cook, R. A. Neiser, T. J. Roemer and D. A. Hirschfeld: *J. Therm. Spr. Tech*, 2006, vol. 15 (2), pp. 233-38.
[16] M. R. Brake: *Int. J. Sol. & Struct*, 2015, vol. 62 pp. 104-23.
[17] T. A. Dewers, J. Heath, R. Ewy and L. Duranti: *Int. J. Oil, Gas & Coal Technology*, 2012, vol. 5 (2/3), pp. 229-48.
[18] L. M. Anovitz and D. R. Cole: *Rev. in Mineralogy & Geochem.*, 2015, vol. 80 pp. 61-164.
[19] J. E. Heath, T. A. Dewers, B. J. O. L. McPherson, R. Petrusak, T. C. Chidsey Jr., A. J. Rinehart and P. S. Mozley: *Geosphere*, 2011, vol. 7 (2), pp. 429-54.

Administrative Addendum

- **Related Publications and Presentations:**

Publications

- D.F. Susan, T.B. Crenshaw, J.S. Gearhart, "The effects of casting porosity on the tensile behavior of investment cast 17-4PH stainless steel", **Journal of Materials Engineering and Performance**, 24, 2917-2923, 2015.

Presentations

- J. Madison, A. Kilgo, E. Huffman, G. Poulter, "R3D at Sandia National Laboratories – A User Update", UES RoboMET.3D™ User's Meeting, Dayton, OH, 15 Sep. 2015, **SAND2015-7665 PE**
- B. Jared, B. Boyce, J. Madison, J. Rodelas, B. Salzbrenner, *"Defect Characterization for Material Assurance in Metal Additive Manufacturing"* International Solid Freeform Fabrication Symposium, Austin, TX, 11 Aug 2015, **SAND2015-6726 C**
- H. Jin, K. Nelson, J. Foulk, **J. Madison,** D. Susan, A. Gu, *"Porosity and Mechanical Characterization of Laser Welds"* SEM 2015 Annual Conference and Exposition, Costa Mesa, CA, 9 June 2015, **SAND2015-0420 A**
- F. Abdeljawad, C. Battaile, J. Bishop, B. Boyce, L. Brewer, J. Carroll, B. Clark, J. Emery, R. Field, J. Foulk, H. Lim, **J. Madison,** S. Owen, "Statistical Descriptions of Defect-Mediated Structure-Properties Relationships in Metals" TMS 2015, Orlando, FL, 18 Mar 2015, **SAND2015-2103 C**

Posters

- J. Madison, E. Huffman, A. Kilgo, G. Poulter, "RoboMET.3D™ @ Sandia National Laboratories; A Unique System, A Unique Capability" US Senate Committee on Appropriations; SEWD Sub-Committee Visit, Albuquerque, NM 19 Aug 2015, **SAND2015-6966**
- B. Jared, B. Boyce, J. Madison, J. Rodelas, "Material Assurance in Metal Additive Manufacturing" Advanced Qualification of Additive Manufacturing Using In-Situ Sensors, Diagnostics & Modeling, Sante Fe, NM, 20 Jul 2015, **SAND2015-5602 C**
- E. Huffman, A. Kilgo, G. Poulter, J. Madison, "RoboMET.3D™ @ Sandia National Laboratories; A Unique System, A Unique Capability" Rio Grande Symposium on Advanced Materials, Albuquerque, NM 6 Oct 2015, **SAND2014-17452 D**

- **Milestone Status:**

Deliverable	Target Date	Status
1. 3D reconstruction and statistical analysis of micro-Ct generated data in laser weld porosity under mechanical loading	FY15Q2 - (3/31/2015)	**COMPLETED**
2. High resolution mechanical serial-sectioning, 3D reconstruction and statistical analysis of tension induced void field in high purity bcc Ta	FY15Q3- (6/30/2015)	**DELAYED TO FY16**
3. High resolution mechanical serial-sectioning, 3D reconstruction and analysis of porosity in thermal spray-coatings on metallic substrates	FY15Q3 - (6/30/2015)	**COMPLETED**
4. High resolution mechanical serial-sectioning, 3D reconstruction and statistical analysis of Iron disulfide in thermal battery cathode	FY15Q3 - (6/30/2015)	**CANCELLED**
5. Infrastructure support for RoboMET.3D™ system (e.g. consumables, technique development, and system customization for non-aqueous serial-sectioning)	FY15Q4 - (9/30/2015)	**COMPLETED**